ADVANCED MATERIALS
www.advmat.de

Defect-Promoted Ni-Based Layer Double Hydroxides with Enhanced Deprotonation Capability for Efficient Biomass Electrooxidation

*Yuwei Yang, William Hadinata Lie, Raymond R Unocic, Jodie A Yuwono, Malte Klingenhof, Thomas Merzdorf, Paul Wolfgang Buchheister, Matthias Kroschel, Anne Walker, Leighanne C. Gallington, Lars Thomsen, Priyank V Kumar, Peter Strasser, Jason A Scott, and Nicholas M Bedford**

Ni-based hydroxides are promising electrocatalysts for biomass oxidation reactions, supplanting the oxygen evolution reaction (OER) due to lower overpotentials while producing value-added chemicals. The identification and subsequent engineering of their catalytically active sites are essential to facilitate these anodic reactions. Herein, the proportional relationship between catalysts' deprotonation propensity and Faradic efficiency of 5-hydroxymethylfurfural (5-HMF)-to-2,5 furandicarboxylic acid (FDCA, FE_{FDCA}) is revealed by thorough density functional theory (DFT) simulations and atomic-scale characterizations, including in situ synchrotron diffraction and spectroscopy methods. The deprotonation capability of ultrathin layer-double hydroxides (UT-LDHs) is regulated by tuning the covalency of metal (M)-oxygen (O) motifs through defect site engineering and selection of M^{3+} co-chemistry. NiMn UT-LDHs show an ultrahigh FE_{FDCA} of 99% at 1.37 V versus reversible hydrogen electrode (RHE) and retain a high FE_{FDCA} of 92.7% in the OER-operating window at 1.52 V, about 2× that of NiFe UT-LDHs (49.5%) at 1.52 V. Ni–O and Mn–O motifs function as dual active sites for HMF electrooxidation, where the continuous deprotonation of Mn–OH sites plays a dominant role in achieving high selectivity while suppressing OER at high potentials. The results showcase a universal concept of modulating competing anodic reactions in aqueous biomass electrolysis by electronically engineering the deprotonation behavior of metal hydroxides, anticipated to be translatable across various biomass substrates.

1. Introduction

The prevalent environmental and energy issues in fossil fuel-related industries have prompted the rapid growth of emerging renewable energy economies and associated technologies. Renewable energy powered electrocatalytic hydrogen production from biomass is emerging as promising next-generation technology in this portfolio, which maximizes the usage of renewable power by converting biomass into fuels and commodity chemicals at the anode while efficiently producing green hydrogen at the cathode.[1] Among prospective biomass oxidation reactions, the 5-hydroxymethylfurfural oxidation reaction (HMFOR) to FDCA holds great promise to substitute the sluggish OER for higher-efficiency energy conversion.[2] Further, FDCA is listed as one of the "top 10" value-added chemicals highlighted by the U.S. Department of Energy (D.O.E), which is a versatile candidate for producing biobased polymers and a range of other derivatives used in plastic industries, pharmaceuticals and fuels.[3]

Y. Yang, W. H. Lie, P. V Kumar, J. A Scott, N. M Bedford
School of Chemical Engineering
University of New South Wales
Sydney, NSW 2052, Australia
E-mail: n.bedford@unsw.edu.au

The ORCID identification number(s) for the author(s) of this article can be found under https://doi.org/10.1002/adma.202305573

DOI: 10.1002/adma.202305573

R. R Unocic
Center for Nanophase Materials Sciences
Oak Ridge National Laboratory
Oak Ridge, Tennessee 37831, USA

J. A Yuwono
School of Chemical Engineering
The University of Adelaide
Adelaide, SA 5005, Australia

M. Klingenhof, T. Merzdorf, P. W. Buchheister, M. Kroschel, P. Strasser
Department of Chemistry
Chemical Engineering Division
Technical University Berlin
10623 Berlin, Germany

Among the reported nonnoble metal electrocatalysts, numerous Ni-based hydroxides have been widely investigated as HMFOR electrocatalysts delivering high selectivity of HMF conversion to FDCA in alkaline aqueous systems and reasonable Faradic efficiency toward FDCA (FE_{FDCA}) at selected potentials.[4] Despite encouraging progress to date, FE_{FDCA} generally declines with increased selected working potentials due to the competition of OER at nonselective active sites. To maximize FDCA production and realize high-rate hydrogen generation, an eminently lower onset potential and high selectivity toward HMFOR in an enlarged potential window are required, especially when considering the need for high reaction rates (and thus higher voltages) associated with the projected industrial-scale output at cathodes and anodes. To date, regulating and enhancing the selectivity of HMFOR toward the competing OER across a range of working potentials remains a challenge. As such, understanding the reaction mechanism of HMFOR on the representative Ni-based hydroxides and how the underlying atomic-scale structure influences this reaction mechanism is crucial for their expanded use under multiple practical conditions.

The fundamentals of proton and electron transfer processes in the electrooxidation of primary alcohol/aldehyde-containing organic molecules on $Ni(OH)_2$ catalysts in alkaline media have been previously explored.[5] The consensus is that the electrodeprotonated Ni hydroxide catalyst is the active phase that serves as a proton and electron acceptor in a spontaneous alcohol/aldehyde dehydrogenation reaction, which consequently gets reduced into its original form.[6] A high intrinsic deprotonation propensity in the catalyst is thus desirable to provide abundant active sites for HMFOR while mitigating OER. Therefore, insights into the electron and proton transfer processes involved in these reactions and regulating the deprotonation capability of Ni hydroxide-based catalysts are needed to achieve kinetically favorable HMFOR, yet studies exploring such vital processes are limited to date.[5e,7] Furthermore, the coupling of the atomic-scale structure of materials during catalysis and the understanding of active structure's influence on deprotonation capability is not well elucidated, leaving a void in structure–activity relationship exploration for these well-studied materials.[8]

Layered double hydroxides (LDHs) are rapidly growing into a prominent family of catalytic materials showcasing high HMFOR activity arising from their easily regulated electronic and interfacial structures, abundant accessible active sites, large specific surface areas, and preferable electron transfer.[4b,9] NiFe LDHs are one of the most well-studied materials for anodic oxidation reactions in alkaline aqueous systems given their excellent performance, especially for OER.[10] NiMn LDH, conversely, is not as well reported for anodic electrocatalysis, although it does have redox properties that are attractive in electrodes for supercapacitors and batteries.[11] In the context of HMFOR, NiMn can potentially provide more deprotonated sites during the electrooxidation of alcohols and aldehydes in HMF, as Mn has a higher redox capability compared with Fe and ready access to a higher valence state.[12]

Herein, we report on a series of Ni-based UT-LDHs consisting of NiFe and NiMn as the metal constituents. The as-prepared ultrathin NiMn LDHs (denoted as UT-NiMn) demonstrate a much lower onset potential at 1.3 V versus reversible hydrogen electrode (RHE) and an ultrahigh Faradic efficiency toward FDCA (FE_{FDCA}) of nearly 100% at 1.37 V. At potentials beyond the OER-operating window, exceptional FE_{FDCA} (92.7% at 1.52 V) is demonstrated, far outperforming commonly used ultrathin NiFe LDHs (UT-NiFe). A suite of atomic-scale characterization techniques combined with theoretical simulations is performed to reveal the origin of catalytic activity and concomitantly offer a critical contextualization of the catalytic behaviors of UT-LDHs during HMFOR and OER. Potential-dependent electrochemical impedance spectroscopy (EIS) and in situ high-energy X-ray diffraction (HE-XRD) coupled with pair distribution function (PDF) analysis confirm that the high selectivity and fast kinetics of UT-NiMn for HMFOR originate from its high deprotonation propensity which stimulates the proton and electron transfer process during the reaction. Further, near-edge X-ray absorption fine structure (NEXAFS) results and DFT calculations verify that the facilitated deprotonation process of UT-NiMn is attributed to the higher covalence of M–O bonds due to the enhanced electron transfer in defective structures. Finally, in situ X-ray absorption near-edge structure (XANES) reveals elementary-sensitive electronic structure changes triggered by the catalysts' interaction with HMF and intermediates. Altogether, we can conclude that the simultaneous deprotonation of Ni–OH and Mn–OH active sites in UT-NiMn catalysts offers more abundant active sites as proton and electron acceptors, facilitating the hydrogen atom transfer (HAT) and electron–proton transfer (EPT) processes in HMFOR for aldehyde and alcohol groups, respectively. Importantly, competing OER reactions are mitigated via the fast $MnOOH\text{-}MnO_2$ structural equilibrium at high potentials. The work provides new insights into the development and application of Ni-based electrocatalysts with ultrahigh selectivity and reactivity in aqueous biomass electrolysis systems. Moreover, the in-depth understanding of the fundamental structural science driving desirable HMFOR reactivity demonstrated here is presumed to provide a roadmap for future catalyst development for organic molecule oxidation and high value added product synthesis, helping meet global goals in efficient sustainable energy generation and large-scale production of fuels and commodity chemicals.

2. Morphological and Structural Understanding of Defective UT-LDHs

The UT-LDHs were prepared by the previously reported coprecipitation method in formamide and water solutions, combined with a subsequent ultrasonication treatment.[13] Formamide, a highly polar solvent, was utilized for synthesis to inhibit layer stacking during growth, where ultrasonic treatment was conducted to obtain near single layer LDHs. The conventional LDHs

A. Walker
US Army DEVCOM Chemical Biological Center
Aberdeen Proving Grounds, MD 21010, USA
L. C. Gallington
X-Ray Science Division
Argonne National Laboratory
Argonne, IL 60439, USA
L. Thomsen
Australian Synchrotron
Australian Nuclear Science and Technology Organisation
Clayton, VIC 3168, Australia

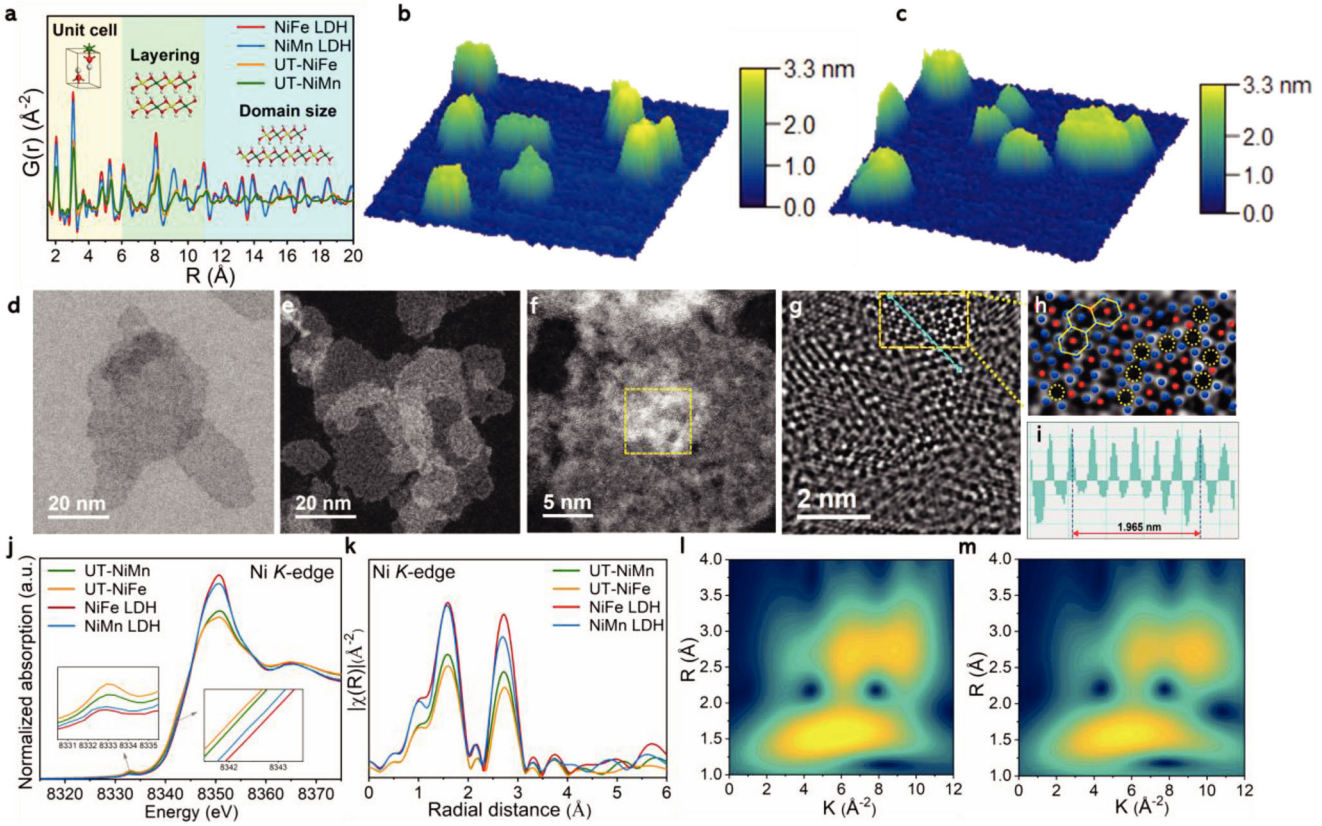

Figure 1. a) Pair distribution functions (PDFs) of NiFe layered double hydroxide (LDH), NiMn LDH, UT-NiFe, and UT-NiMn; 3D atomic force microscopy (AFM) images of b) UT-NiMn and c) UT-NiFe. d) Bright-field scanning transmission electron microscopy (STEM) image of UT-NiMn. e,f) Dark-field STEM image of UT-NiMn. g) Inverse fast Fourier transform (FFT) of the selected square region in (f). h) The zoomed-in diagram of the selected yellow region in (g), for a clearer demonstration of the existence of distorted structure and metal vacancies (blue and red spheres represent Ni and Mn atoms, and yellow hollow dash represents metal vacancies, distorted hexagon represents the distortions in the structure, oxygen atoms are not visible in DF-STEM images). i) Line profile for the selected line in its inverse FFT image indicating the expanded lattice structure due to the existence of oxygen vacancies. j,k) Ni K-edge X-ray absorption near-edge structure (XANES) and edge X-ray absorption fine structure (EXAFS) spectra of NiMn LDH, NiFe LDH, UT-NiMn, and UT-NiFe; WT contour of Ni K-edge of l) UT-NiMn and m) UT-NiFe.

were fabricated by a typical coprecipitation method for subsequent control experiments (see Supporting Information).[14] Comprehensive characterization techniques, including powder XRD (PXRD), high-resolution transmission electron microscopy (HR-TEM), HE-XRD coupled with PDF analysis, and atomic force microscopy (AFM), were used to verify the successful synthesis of UT-LDHs contrasted against coprecipitated LDHs. The PXRD patterns of NiFe and NiMn LDHs show two basal plane peaks at $2\theta = 11.38°$ (8.09 $Å^{-1}$) and 22.93° (16.22 $Å^{-1}$), corresponding to the (003) and (006) lattice planes of typical layered hydrotalcite structures (Figure S1, Supporting Information).[15] In contrast, very small and broad peaks can be observed at the same position in the patterns of UT-NiFe and UT-NiMn, ascribed to the limited ability of UT-LDHs to re-stack layers during the drying process.[16] Additionally, the absence of diffraction peaks, including the (110) plane peak of the *ab*-plane, is observed in the PXRD pattern, indicating a more disordered structure of UT-LDHs with reduced lateral size.[17] HE-XRD data coupled with PDF analysis further confirms the successful synthesis of UT-LDHs, providing atomic-scale structural information in real space by converting the total scattering extracted from HE-XRD data into a function of coordination spheres exceeding 20 Å in the material (**Figure 1**a).[18] The PDF of UT-LDHs exhibits decreased peak intensities and short-range order within 12 Å (the region of unit cells and layering), deriving from more disordered structures in ultrathin materials.[19] Additionally, the long-range order is further impacted by intrinsically more abundant defects and the reduced height and lateral size of UT-LDHs.[20] The topology of UT-LDHs was examined by AFM, demonstrating well-distributed nanosheets with an average height of 2–3 nm (Figure 1b,c; Figures S2 and S3, Supporting Information). In contrast, a series of LDHs prepared by the traditional coprecipitation method feature hierarchical structures with a total size of ≈500 nm and a thickness of 10–15 nm (Figures S4 and S5, Supporting Information). High-angle annular dark-field scanning TEM (HAADF–STEM) images of UT-LDHs illustrate uniformly dispersed nanosheets with lateral sizes of around 20–40 nm (Figure 1d–f; Figures S6 and S7, Supporting Information). Fast Fourier transform (FFT) and inverse FFT analyses were applied to reveal an atomic structural understanding of the selected area (Figure 1g; Figure S8, Supporting Information), showing limited short regions with ordered lattice fringes,

while the other selected areas are more disordered in nature. The presence of distorted hexagonal coordinates and the partial absence of metal sites clearly reveal structural distortions and metal vacancies in the UT-LDHs (Figure 1h; Figure S9, Supporting Information); further, the existence of oxygen defects is identified by the line profile along the (0012) edge plane of UT-NiMn nanosheets (Figure 1i). Compared with the nondefective NiMn LDHs with a d_{0012} of 0.258 nm, the d_{0012} of UT-NiMn is 0.327 nm, revealing an expanded lattice due to localized oxygen deficiency.[21]

The presence of oxygen defects was further examined by a series of XAS techniques. The Ni K-edge XANES spectra of UT-NiMn and UT-NiFe are shown in Figure 1j. UT-LDHs show lower E_0 and decreased white line intensity compared with the LDHs prepared by coprecipitation methods, revealing the changed electronic structure of Ni atoms due to copious oxygen defects. The free electrons accompanying the oxygen defects localize to the nearby Ni, leading to the formation of electron-rich $Ni^{(2-n)+}$ (n = number of free electrons generated from oxygen defects).[22] Furthermore, both NiMn and NiFe UT-LDHs show the increased intensity of the pre-edge features (inset in Figure 1j), where the pre-edge feature is a reflection of the dipole forbidden 1s to 3d transition. The deviated centrosymmetry in distorted and oxygen-defect-rich UT-LDHs allows more metal 3d and 4p mixing and in turn amplifies the pre-edge intensity.[22] Similarly, the XANES spectra of Mn K-edge and Fe K-edge present the same trend (Figure S10, Supporting Information), implying the existence of oxygen defects throughout UT-LDHs. The element-specific local structure of UT-LDHs is revealed by EXAFS (Figure 1k; Figure S11, Supporting Information). The Ni K-edge EXAFS exhibits two peaks at 1.6 Å for the first coordination shell and 2.7 Å (without phase correction) for the second coordination shell, corresponding to Ni–O and Ni–M, respectively. Both peak intensities are decreased due to the decisive effect of unsaturated oxygen and metal sites near Ni atom, further showcasing a disordered in-plane LDH structure. Further, the co-existence of the two metals at Ni–M position in both UT-LDHs and LDHs is verified by wavelet transform (WT) of Ni K-edge EXAFS spectra, respectively, in which two hotspots in high k-space can be observed at 2.7 Å (Figure 1l,m; Figures S12 and S13, Supporting Information). Compared with conventional LDHs, decreased intensity is also observed at the Fe–O and Fe–Fe(Ni) peaks in Fe K-edge EXAFS spectra and the Mn–O and Mn–Mn(Ni) peaks in Mn K-edge EXAFS spectra of UT-LDHs, respectively (Figure S11, Supporting Information). Interestingly, the Mn K-edge EXAFS spectra of both NiMn LDHs and UT-NiMn display a shorter Mn–O bond at 1.4 Å and an additional peak at 3.3 Å, which is a consequence of JT distortion near the Mn site in Mn-containing systems.[23] The defective structure of UT-LDHs is further validated by fitting the EXAFS spectra of respective edges; importantly, the detailed fitting results reveal an obvious reduction in the coordination numbers of M–M and M–O bonds (Tables S1 and S2 and Figures S14–S17, Supporting Information).

3. Catalytic Performance and Kinetics Analysis

The electrocatalytic performance of UT-LDH and conventional LDH catalysts were evaluated by linear sweep voltammetry (LSV) measurements in 1 M KOH with and without 10×10^{-3} M HMF. As shown in Figures S18 and S19 (Supporting Information), both UT-NiMn and UT-NiFe electrocatalysts exhibit substantially enhanced OER and HMFOR catalytic performances compared to their LDH counterparts. In particular, for HMFOR, UT-NiMn and UT-NiFe show 146 and 57 mV lower overpotentials than their corresponding LDHs at a current density of 40 mA cm^{-2}, respectively. Interestingly, UT-NiMn and NiMn LDHs show a large HMFOR versus OER potential gap of 200 and 97 mV at 40 mA cm^{-2}, respectively, which are much larger than those of classical UT-NiFe (64 mV) and NiFe LDHs (11 mV) (**Figure 2**a). Lin et al. studied the competition between organic compound oxidation reactions (OCOR) between OER by a series of electrochemical methods, and it was found that the detrimental OCOR/OER competition region of catalysts starts near the "endpoint" of the catalyst oxidation features.[24] In our work, under the OER condition, the LSV curve of UT-NiFe shows a sole oxidation feature "a," representing the transition from Ni^{2+} to Ni^{3+}.[7] In contrast, the UT-NiMn shows an additional oxidation feature "b" of Mn^{3+} to Mn^{4+} transition.[25] Thus, the enlarged HMFOR working potential window of the Mn-containing hydroxides is likely due to the introduction of Mn, which delays the happening of competing OER (Figure S18, Supporting Information).

HMF to FDCA conversion was analyzed using high-performance liquid chromatography (HPLC) to track the reaction process and possible intermediates involved in the HMFOR (Scheme S1, Supporting Information), and the concentration of FDCA was calculated by using the calibration curve in Figure S20 (Supporting Information). As illustrated in Figure S21 (Supporting Information), the charge consumption on the catalysts shows a positive linear relationship with the FDCA concentration and a negative linear relationship with the HMF concentration. UT-LDHs reach the reaction endpoint within 70 min, around one-third of the reaction time of coprecipitated LDHs. Moreover, the plots of ln[HMF] versus time for each anode illustrate a linear trend (Figure S22, Supporting Information), suggesting a first-order reaction rate for HMF consumption. The rate constants follow the order $K_{\text{UT-NiMn}}$ (0.081 ± 0.003 s^{-1}) > $K_{\text{UT-NiFe}}$ (0.067 ± 0.003 s^{-1}) > $K_{\text{NiMn LDH}}$ (0.028 ± 0.003 s^{-1}) > $K_{\text{NiFe LDH}}$ (0.011 ± 0.001 s^{-1}), suggesting the fastest HMFOR kinetics are present on UT-NiMn. To better understand the electrodynamic process during the HMFOR, a charge-time (C–T) plot is introduced to assess the charge transfer kinetics on different catalyst surfaces during reaction. The charge transfer kinetics of HMFOR are analyzed using the quasi-linear region (the orange region in Figure 2b) within the first 20 min of conversion to avoid the influence of HMF concentration on the charge transfer kinetics caused by HMF consumption during the reaction. Figure 2b shows that the overall charge transfer rates follow the trend UT-NiMn (6.7 ± 0.2 C min^{-1})> UT-NiFe (3.9 ± 0.1 C min^{-1}) > NiMn LDHs (2.6 ± 0.1 C min^{-1}) > NiFe LDHs (1.7 ± 0.1 C min^{-1}), consistent with the HMFOR kinetics. Both UT-NiMn and NiMn LDHs exhibit a distinct plateau at the end of their C–T plots, closely associated with diffusion-limited HMF concentrations toward the end of the reaction. Despite a reduced charge consumption rate with HMF consumption, UT-NiFe and NiFe LDHs retain relatively high charge consumption rates when the HMF concentration is

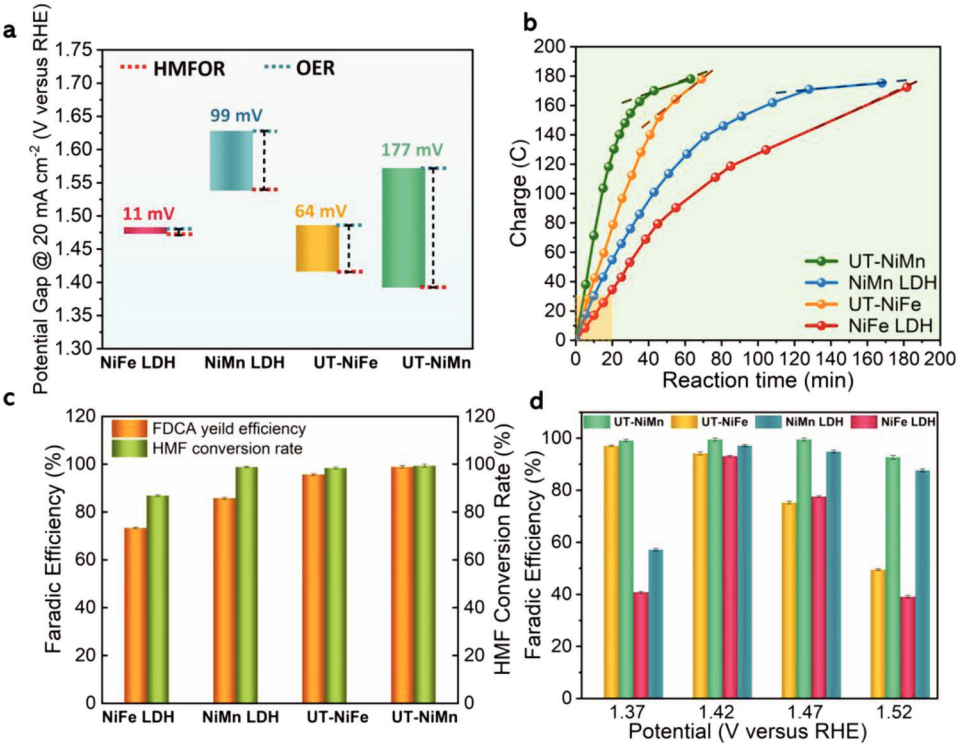

Figure 2. a) 5-Hydroxymethylfurfural oxidation reaction (HMFOR) versus oxygen evolution reaction (OER) potential gap for NiMn layered double hydroxide (LDH), NiFe LDH, UT-NiMn, and UT-NiFe catalysts acquired from linear sweep voltammetry (LSV) curves at a current density of 20 mA cm^{-2}. b) Charge–time plot of NiMn LDH, NiFe LDH, UT-NiMn, and UT-NiFe catalysts during HMFOR using 10×10^{-3} M HMF at an identical current density of 10 mA cm^{-2}. c) HMF conversion rate and FDCA (furandicarboxylic acid) yield faradic efficiency by NiMn LDH, NiFe LDH, UT-NiMn, and UT-NiFe in 1 M KOH + 10×10^{-3} M HMF. d) Potential-dependent FE_{FDCA} of NiMn LDH, NiFe LDH, UT-NiMn, and UT-NiFe in 1 M KOH + 10×10^{-3} M HMF.

at a lower level (even at the end of the reaction), indicating the co-occurrence of HMFOR and OER on Fe-containing hydroxide catalysts.

The HMF-to-FDCA conversion performance of UT-LDHs and LDHs follows the same order of UT-NiMn > UT-NiFe > NiMn LDH > NiFe LDH (Figure 2c), among which UT-NiMn displays the best HMFOR performance with a FE_{FDCA} of nearly 100%. As FDCA is the only final product observed from the chromatic graphs (Figure S23, Supporting Information), the relatively large difference between the HMF conversion rate and FE_{FDCA} of conventional LDHs is caused by the degradation of HMF under strongly alkaline conditions after a long reaction period.[26] Importantly, when coupled with the hydrogen evolution reaction for high-rate production of hydrogen and value-added products, decent FE_{FDCA} is observed for UT-NiMn at higher potentials which are especially desirable. Thus, instead of testing the catalysts at low potentials to purposely avoid the OER region, the HMF conversion performance at different potentials is screened (Figure 2d; Table S3, Supporting Information). UT-NiMn exhibits a superior FE_{FDCA} (>95%) across a large potential window, ranging from 1.37 to 1.47 V, and retains a high FE_{FDCA} (92%) at a high potential (1.55 V). In contrast, UT-NiFe and NiFe LDHs only show a high FE_{FDCA} at potentials of 1.42 V or lower. Overall, the results indicate that the charge transfer kinetics, HMFOR kinetics, and FE_{FDCA} of UT-LDHs are significantly improved compared to traditional LDHs. UT-NiMn catalysts offer better performance than UT-NiFe under the considered test conditions and display particularly superior selectivity toward HMFOR in all studied potentials.

4. Structural–Activity Relationship Revealed HMFOR-OER Competition

In situ HE-XRD coupled with PDF analysis was conducted on LDHs and UT-LDHs under OER and HMFOR conditions to gain insights into their dynamic structural transformation and correlation with the different electrocatalytic performances. All electrodes were precycled using CV method to acquire the stabilized catalyst surface prior to the experiments under different conditions. Under the OER condition, coprecipitated NiFe LDHs do not undergo an obvious structural change at applied potentials (Figure S24, Supporting Information). The two predominant peaks at 2.06 and 3.08 Å are assigned to Ni(Fe)–O and Ni(Fe)–Fe(Ni) of the typical hydroxide structure, respectively. Similarly, the coprecipitated NiMn LDHs display a stabilized structure with applied potential (Figure S24, Supporting Information). In contrast, the UT-NiFe catalysts show unambiguously structural changes across the PDFs, whereby the Ni(Fe)–O peak shifts from 2.04 to 1.85 Å and the Ni(Fe)–Fe(Ni) peak shifts from 3.08 to 2.82 Å under the applied potentials. This occurs in conjunction with the peak positions being shifted at longer pair distances, suggesting a full structural transformation

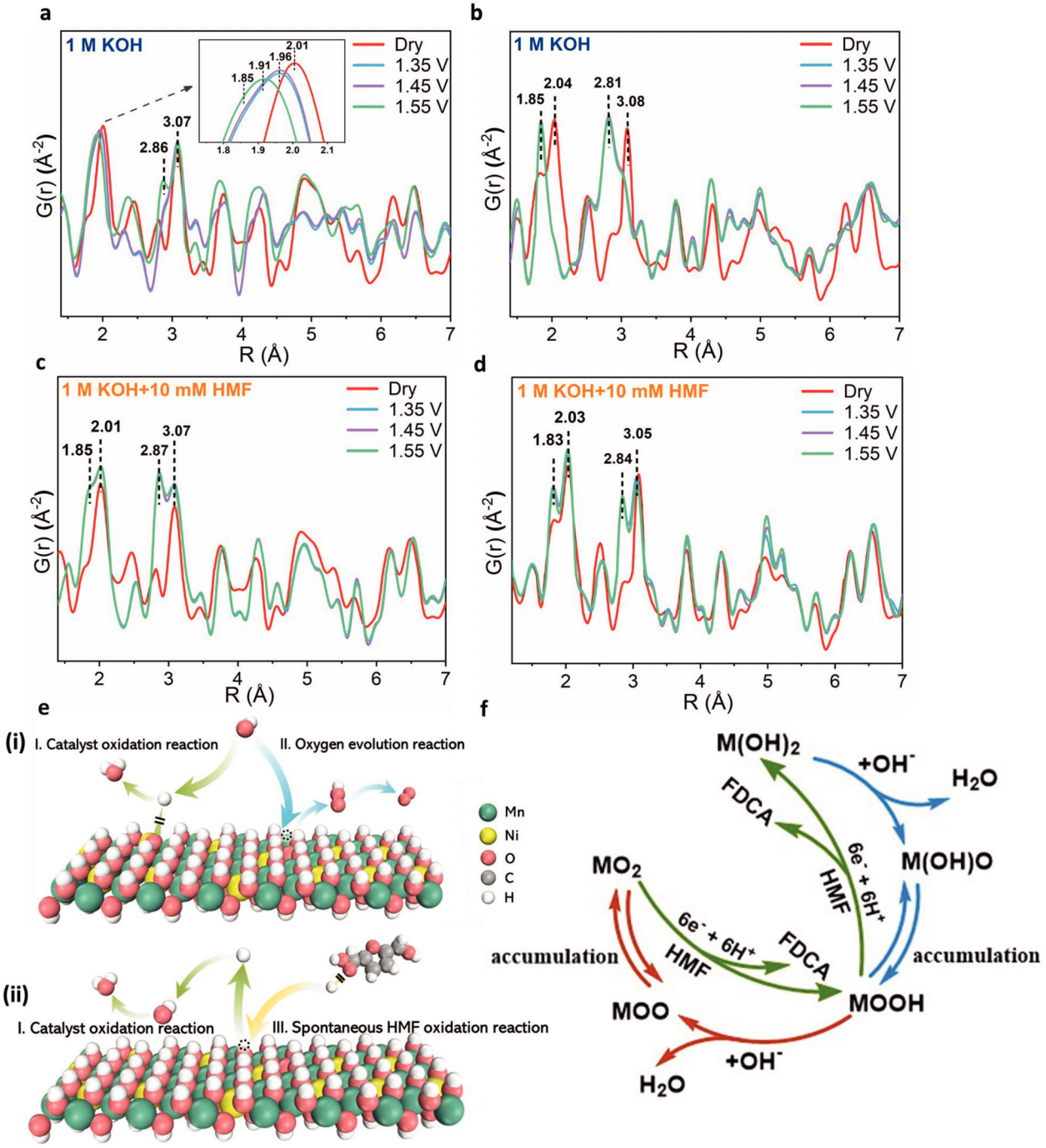

Figure 3. Atomic pair distribution functions (PDFs) of a) UT-NiMn and b) UT-NiFe in pure 1 M KOH. c) UT-NiMn and d) UT-NiFe in 1 M KOH + 10×10^{-3} M HMF. e) Schematic diagram of i) the competition between catalyst deprotonation reaction and oxygen evolution reaction (OER) (top) and ii) the reaction mechanism of deprotonated catalyst sites as electron and proton acceptors for 5-hydroxymethylfurfural oxidation reaction (HMFOR) (bottom). f) Involved structural transformation and structure regeneration process of Ni-based layered double hydroxides (LDHs) during OER and HMFOR.

from hydroxides to oxyhydroxides under OER conditions (**Figure 3**a).[19,27] In contrast, UT-NiMn provides different in situ structural changes (Figure 3b), which are attributed to different degrees of deprotonation propensity for Ni–O and Mn–O sites under applied potential. At applied potentials of 1.35 and 1.45 V under OER conditions, UT-NiMn shows a broad peak consisting of two merged peak features centered at 1.85 and 1.96 Å, which are assigned to Ni–O and Mn–O bonds of NiOOH and JT-distorted MnOOH, respectively.[28] For applied potentials up to 1.55 V, a further decrease in M–O bond length to 1.91 Å is observed, which is assigned to the Mn–O peak in a MnO_2-like structure due to the further deprotonation of Mn–O sites

in MnOOH.[28b,29] A scheme depicting the dynamic redox process between MnOOH and MnO_2 has been frequently reported for Mn-based catalysts during the OER (Scheme S2, Supporting Information).[30] Under HMFOR conditions, the coprecipitated LDHs show a stabilized structure similar to under OER conditions, while UT-LDHs collectively demonstrate new features representing their reduced-state structures. UT-NiFe attains well-split features of hydroxides and oxyhydroxides (Figure 3c), uncovering that both structural motifs are observable during HMFOR. UT-NiMn similarly demonstrates the appearance of multiple structural features, including NiOOH, $Ni/Mn(OH)_2$ and merged features of MnOOH and MnO_2-like structures (Figure 3d). The important differences in structure between OER and HMFOR for UT materials is that the original hydroxide structure is directly observable in the PDFs across all voltages, showcasing HMF's ability to convert the material away from high-valence oxides.

Our findings from in situ PDF measurements demonstrate clear structural change differences under OER and HMFOR conditions, providing key insights into the active site structures and electrocatalytic mechanisms. In pure KOH electrolytes, the catalytic reaction on hydroxides could be simplified into two consecutive processes, namely the catalyst deprotonation reaction (step I) and OER (step II), as shown in Figure 3ei. Specifically, $M(OH)_2$ initially turns into M(OH)O in the dehydrogenation reaction with applied potentials, and the phase transformation of $M(OH)_2 \rightarrow$ MOOH happens subsequently with the accumulation of M(OH)O intermediate (Figure 3f).[5e] Thus, the occurrence of structural transformation depends on the reaction rate constants of step I (k_{depro}) and step II (k_{O2}). When $k_{depro} >> k_{O2}$, the hydroxide catalyst rapidly transforms into its oxyhydroxides (and potentially high valence oxides) with a fast accumulation of deprotonated intermediates, as shown in Figure 3f; however, when $k_{depro} << k_{O2}$, the rapid release of O_2 inhibits the further accumulation of deprotonated Ni(OH)O and structural evolution does not occur.[31] As structural transformation is only observed in UT-LDHs, while LDHs remain a stable structure with applied bias, it can be concluded that UT-LDHs have a higher propensity for deprotonation rather than direct OER compared to traditional LDHs, of which UT-NiMn shows the highest level of deprotonation according to its final in situ state. Importantly, the trend toward deprotonation propensity strongly correlates to the previously observed trend of the catalysts' FE_{FDCA} performance and selectivity toward HMFOR. Additionally, structure stabilization observed with the presence of HMF validates the redox reaction mechanism between HMF and hydroxide-based catalysts, of which biomass substrates transfer protons and electrons to electrogenerated oxyhydroxides/oxides and convert the catalyst to their reduced states (Figure 3eii). Thus, the universal high selectivity of UT-NiMn toward HMFOR over a broad potential range is likely related to its higher deprotonation propensity. This is especially the case at Mn–OH sites, where continuous catalyst oxidation on these sites delays the occurrence of OER, and the more oxidized Mn–O sites may be able to accept two protons and electrons from HMF and its intermediates by reducing from MnO_2 to MnOOH and finally to $Mn(OH)_2$.

Overall, according to the "indirect oxidation" scheme of HMF, where the oxidation of HMF and its intermediates spontaneously occurs on the electrogenerated electrocatalysts, HMFOR could be considered a simple chemical reaction involving two categories of reactants: the proton and electron from HMF and its intermediates, and deprotonated M–O sites (Schemes S2 and S3, Supporting Information).[9b] As the HMF concentration is high enough, an elevated concentration of deprotonated M–O active sites is desired for highly active and efficient HMF conversion. Thus, combined with the catalyst performances of HMF-to-FDCA conversion in the previous section, an estimation could be made that a high k_{depro} is desired to achieve enhanced HMFOR performance. In addition, the competition between the HMFOR and OER originates from competition between the catalyst deprotonation reaction and OER. Thus, to fulfill high selectivity toward HMFOR over the competing OER, a reaction rate of $k_{depro} > k_{O2}$ is especially preferred. The structure stability of the UT-LDHs and LDHs after OER and HMFOR was further examined by postreaction XRD, XAS, and NEXAFS (Figures S25–S31, Supporting Information). The PXRD results of the postreaction UT-LDHs show even less prominent features of hydrotalcite than their respective pristine materials, indicating a slightly more disordered structure of the UT-LDHs after catalytic reactions (Figure S25, Supporting Information). Further, the O K-edge XANES of both post-OER UT-LDHs display a peak before 530 eV, indicative of metal oxides, suggesting the emergence of high-valence metal oxyhydroxides or oxides (Figures S28c and S29c, S25c and S26c, Supporting Information).[32] Notably, this feature is absent in post-HMFOR materials, which underscores the redox processes of HMF on the deprotonated catalyst, consistent with our in situ PDF results. The unaltered peaks in Ni and Fe XANES spectra and EXAFS affirm the stable structure and oxidation states of Ni and Fe postreactions. Conversely, the appearance of the shorter M–M peaks at the Mn K-edge and Ni K-edge EXAFS, combined with the adsorption peak shifts in Mn K/L-edge XANES, elucidates an increased oxidation state of Mn, likely due to the partial formation of $MnOOH/MnO_2$; and they may phase separate from the LDH material after sustained electrooxidation.[33] Collectively, postreactions findings suggest a lack of materials degradation for all catalyst tested with stable higher-order oxidization states, with the final catalyst structure reflecting observations from in situ PDF measurements.

5. Understanding the Selectivity Difference Between UT-NiFe and UT-NiMn Toward HMFOR

Potential-dependent EIS was conducted to study the different electrochemical interface behaviors of UT-NiMn and UT-NiFe during OER and HMFOR, providing further evidence on their deprotonation propensity related to HMFOR selectivity. Optimum fit parameters for EIS data and the equivalent circuits used for fittings are presented in Tables S4–S7, Figures S32 and S33 (Supporting Information). In the Bode plot, there are two regions of interest, a low-frequency interface region dominated by mass transfer and a high-frequency interface region dominated by charge transfer.[34] The case of OER (**Figure 4**a,b) is first introduced to establish a rationale between catalyst behavior and its reflection in the Bode plot before discussing HMFOR (Figure 4c,d). Combined with the position of the oxidation peak features in the LSV curves (Figure S18, Supporting Information) of UT-NiFe and UT-NiMn, the appearance of the dominant peak in the mid-high frequency region (10^1–10^5 Hz) of the

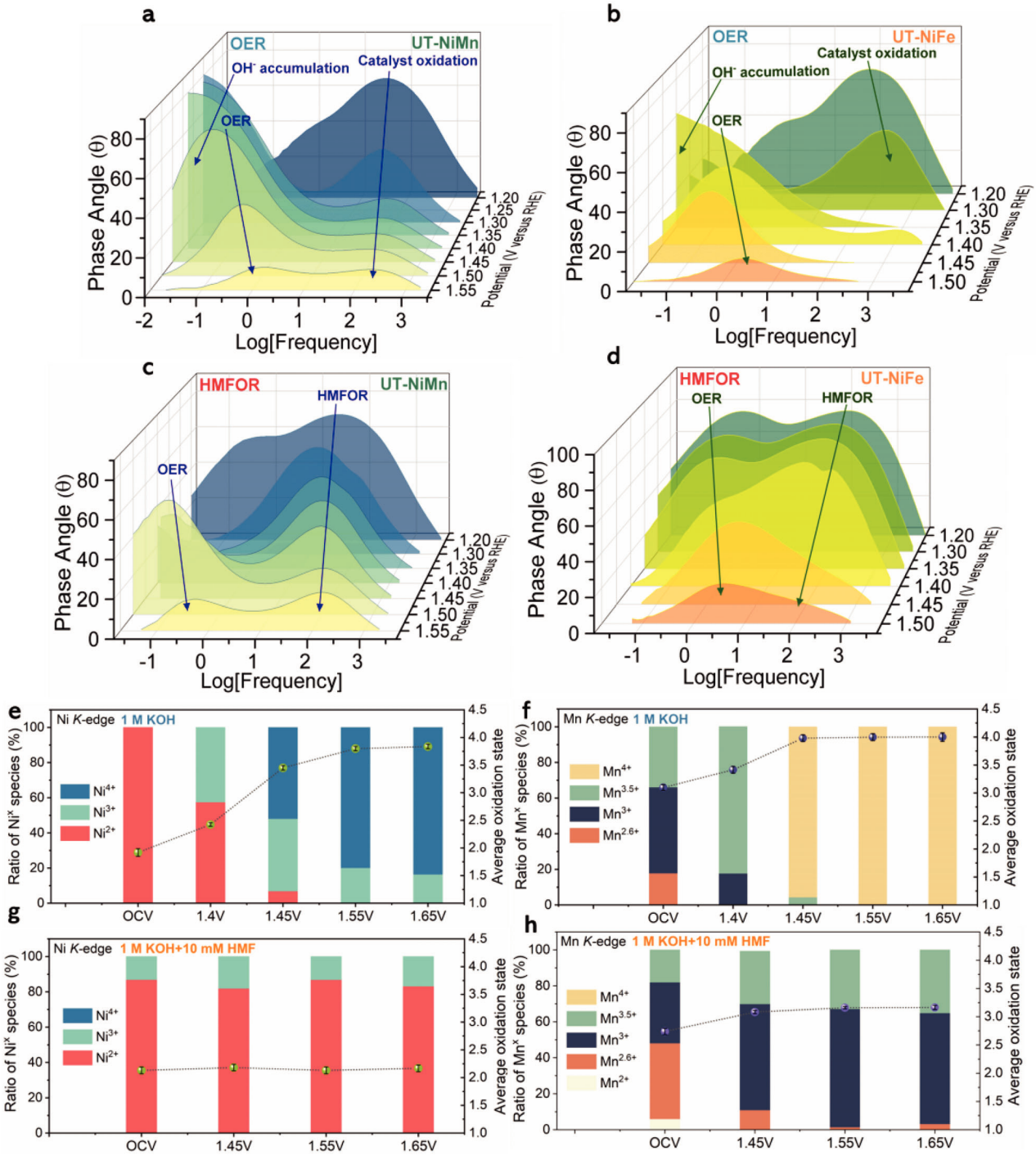

Figure 4. Bode phase plots of in situ electrochemical impedance spectroscopy (EIS) on a) UT-NiMn and b) UT-NiFe in 1 M KOH with 10×10^{-3} M HMF. Bode phase plots of in situ EIS on c) UT-NiMn and d) UT-NiFe in 1 M KOH with 10×10^{-3} M HMF. Optimal liner combination fitting result of the X-ray absorption near-edge structure (XANES) spectra and average oxidation state of e) Ni K-edge of UT-NiMn in 1 M KOH. f) Mn K-edge of UT-NiMn in 1 M KOH. g) Ni K-edge of UT-NiMn in 1 M KOH+10×10^{-3} M HMF. h) Mn K-edge of UT-NiMn in 1 M KOH+10×10^{-3} M HMF.

Bode plots is an indicator of catalyst deprotonation/catalyst surface oxidation. At the same time, with further applied potentials, the plot shows decreased peak intensity in the high-frequency region combined with a growing high-rising end in the ultralow-frequency region ($<10^{-1}$ Hz), representing OH^- accumulation on the catalyst surface for catalyst structural transformation and the OER. The observed increase in intensity with applied potentials is attributed to the increased thickness of the diffusion layer with further accumulated OH^-.[35] With the completed structural transformation at further increasing potentials, the plot

demonstrates a peak in the low-frequency region (10^{-1}–10^{1} Hz), signifying OER onset and the generation of O_2 molecules, which is highly consistent with the ending oxidation peak and sharply rising current density in the LSV curve corresponding to the OER (Figure S18, Supporting Information). Interestingly, the Bode plot of UT-NiMn exhibits a constant peak even at high potentials in the high-frequency region, suggesting a continuous catalyst oxidation reaction even with the occurrence of the OER. This may be explained by the OER reaction mechanism at Mn sites, where a constant equilibrium exists between MnOOH and MnO_2 during the OER (Scheme S2, Supporting Information).

HMFOR is a spontaneous redox reaction that happens on the catalyst surface between HMF/HMF derivatives and the deprotonated catalyst surface. Thus, continuous catalyst electrooxidation is necessary to provide sufficient electron and proton acceptors for the involved proton and electron transfer processes.[36] Under this scenario, the Bode plot of UT-NiMn shows peaks of unremitting catalyst oxidation in the high-frequency region over the full testing range (from 1.2 to 1.55 V), with the OER peak appearing only from 1.5 V and remaining at high intensity. The finding confirms the low involvement of the OER at 1.5 V, which is consistent with the high FE_{FDCA} performance of UT-NiMn, even at 1.55 V. In contrast, UT-NiFe shows a gradual shift of the predominant peak position from the high-frequency region to the low-frequency region. Combined with the reduced potential-dependent FE_{FDCA} performance of UT-NiFe at applied potentials, it can be concluded that OER is more involved than HMFOR at high potentials.

The EIS fitting results of UT-NiMn and UT-NiFe under OER and HMFOR conditions are further compared to give a clearer image of their potential-dependent selectivity performance between HMFOR and OER (Figure S34, Supporting Information). In the equivalent circuit model for EIS fitting, the Rs represent the resistance of the electrolyte, and the R1 and R2 represent the charge transfer resistance and mass transfer resistance, respectively. For UT-NiFe, R1 in the HMFOR system is considerably larger than that in the OER system in the range of 1.3–1.4 V due to the continuous charge consumption on catalyst oxidation, which is simultaneously reduced by biomass substrates. A high FE_{FDCA} is also achieved within this voltage region. The sudden drop in R2 for HMFOR at 1.45 V suggests greater involvement by the OER from this point onwards, at which a marked drop in FE_{FDCA} is also observed. Regarding UT-NiMn under OER conditions, a constant decrease in R1 from 1.3 to 1.4 V is apparent. However, the plot shows an increase in R1 at 1.45 V; at the same time, R2 representing OER also appears, revealing the initiation of the self-redox MnO_2-MnOOH couple involved in the OER. In contrast, a similar hump of R1 is observed at 1.5 V in the HMFOR system, combined with the emergence of R2, further validating that OER begins from this point. Accordingly, the OER will only commence once the catalysts reach their "upper limit" of deprotonation and further OH^- accumulation. The ability of UT-NiMn to further deprotonate facilitates the delay in the OER and broadens the HMFOR working window with better FE_{FDCA}.

In situ XANES was applied to UT-NiMn and UT-NiFe under OER and HMFOR operating conditions to characterize elemental-specific catalyst deprotonation propensity and their roles in determining the HMFOR working window and selectivity at high potentials (Figure 2d). Linear combination fitting was performed on the in situ XANES spectra of Ni K-edge, Mn K-edge, and Fe K-edge to acquire the weighted average oxidation states (Figures S35–S42, Supporting Information). The Ni in UT-NiFe has a slightly higher oxidation state (1.77) than for UT-NiMn (1.65). In a pure 1 M KOH electrolyte, the Ni valence state in UT-NiFe gradually increases and reaches its final oxidation state (3.80) at 1.45 V (Figure S43a, Supporting Information). The valence state of Ni in UT-NiMn reaches its highest oxidation state (3.84) when the applied potential reaches 1.55 V (Figure 4e). The potentials of the above-observed equilibrium oxidation states are consistent with the respective "endpoint" of the oxidation feature at around 1.45 V of UT-NiFe and 1.55 V of UT-NiMn, as seen in the polarization curves (Figure S18, Supporting Information). Interestingly, the Fe in UT-NiFe exhibits a generally stabilized oxidation state (2.85) across the reaction range (Figure S43b, Supporting Information), suggesting no catalyst deprotonation has occurred on Fe–OH sites.[10e] The Mn in UT-NiMn has an initial oxidation state of 2.62 and reaches its stabilized highest oxidation state (3.98) at 1.45 V (Figure 4f). Under the HMFOR condition, the Ni in both UT-LDHs remains stabilized as Ni^{2+} across the entire tested ranges, and the Fe in UT-NiFe remains stable at the oxidation state of 2.88 at all potentials (Figure 4g; Figure S43c,d, Supporting Information). However, the Mn in UT-NiMn displays an increased oxidation state even in the presence of HMF, implying a higher rate of catalyst deprotonation than the rate of the spontaneous HMFOR on Mn–O active sites (Figure 4h). As discussed previously, the HMFOR working window is closely related to the potential window of catalyst deprotonation, and the essence of the competition between HMFOR and OER is the competition between catalyst deprotonation and the OER. Thus, the UT-NiMn with a larger catalyst deprotonation window (up to 1.55 V) and higher catalyst deprotonation propensity on Mn sites possesses a larger working window and higher selectivity toward HMFOR. In contrast, the concurrent catalyst deprotonation on both Ni–OH and Mn–OH sites in UT-NiMn provides more abundant proton and electron acceptors than the UT-NiFe, as no deprotonation is observed on Fe–OH sites.

The pre-edge features of the transition metals' XANES spectra provide information on the quadrupole-allowed dipole-forbidden 1s to 3d excitations. In the 1 M KOH electrolyte, the Ni K-edge and Mn K-edge pre-edge of UT-NiMn and Ni K-edge pre-edge of UT-NiFe illustrate continuous positive shifts due to the increased oxidation state of Ni and Mn, while the Fe K-edge pre-edge remains stable (Figure S44, Supporting Information). Interestingly, in the presence of 10×10^{-3} M HMF, despite a stable pre-edge spectrum of the Ni K-edge of UT-NiFe and UT-NiMn, the pre-edge of the Mn K-edge still shows even further positive shifts with applied potential. This is despite a more stabilized rising edge and adsorption edge of the Mn K-edge, revealing the formation of the electron-deficient Mn at Mn–O sites (Figure S45, Supporting Information). In line with the proposed HAT and EPT reaction mechanisms by Fleischmann et al. and Bender et al. (Scheme S3, Supporting Information), the reaction at Ni–O sites for both UT-LDHs may follow the HAT mechanism, where electrons are transferred to the Ni^{3+}, reducing it back to Ni^{2+}, and protons are transferred to nearby O.[5b,f] In comparison, at Mn–O sites, the reaction follows the EPT reaction mechanism, in which both electrons and protons are transported to nearby O, so that Mn remains electron-deficient with no obvious structural

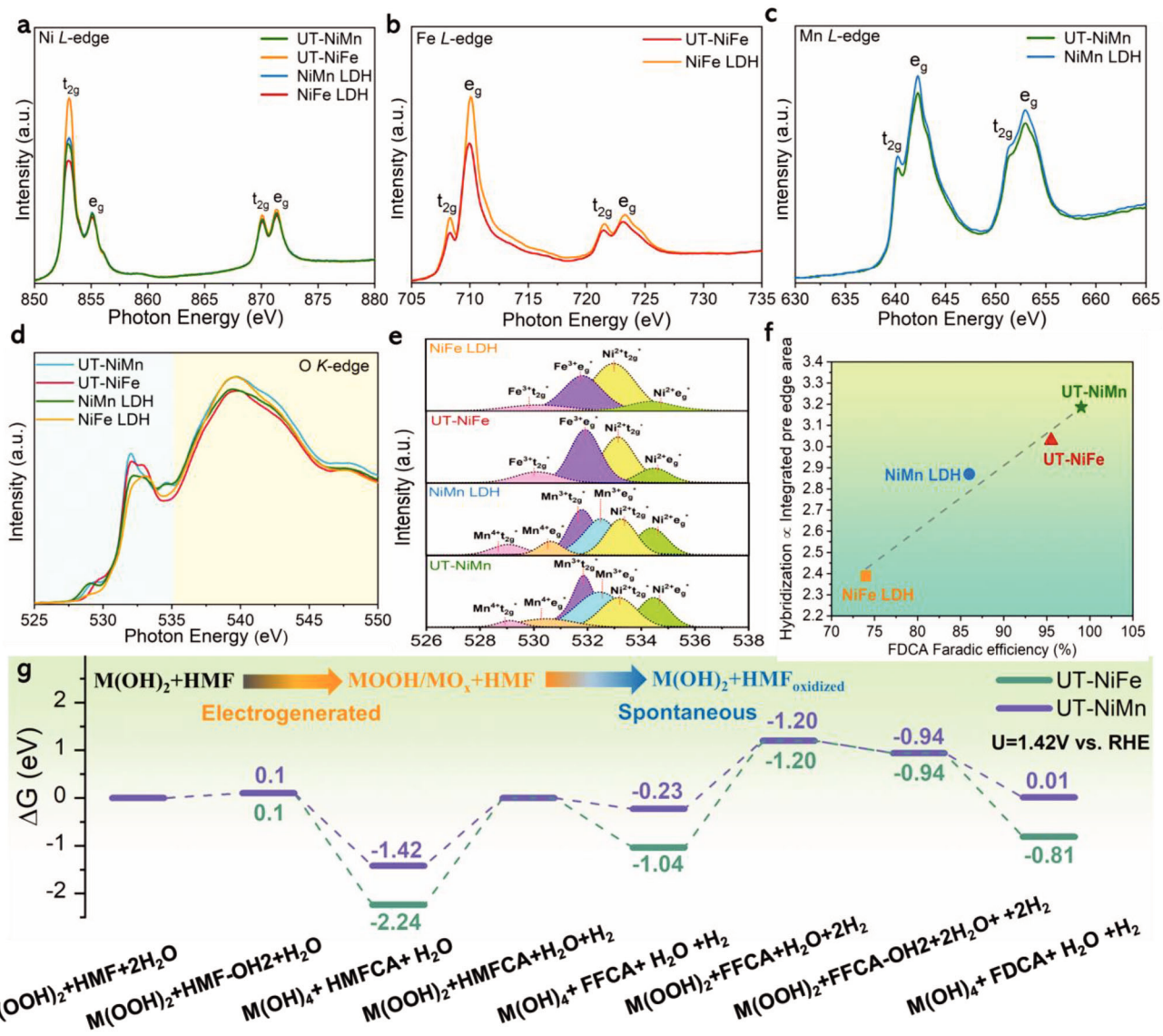

Figure 5. Near-edge X-ray absorption fine structure (NEXAFS) spectra of a) Ni L-edge of UT-NiMn, NiMn layered double hydroxide (LDH), UT-NiFe, and NiFe LDH. b) Fe L-edge of UT-NiFe and NiFe LDH. c) Mn L-edge of UT-NiMn and NiMn LDH. d) O K-edge of UT-NiMn, NiMn LDH, UT-NiFe, and NiFe LDH (blue region represents the pre-edge region of O K-edge spectra). e) The fitted pre-edge of O K-edge of UT-NiMn, NiMn LDH, UT-NiFe, and NiFe LDH. f) Liner trend of the covalence/hybridization level of catalyst from the integrated area of O 2p and M 3d hybridization in the O K-edge versus catalyst FE_{FDCA} performance. g) Density functional theory (DFT) calculated energy profiles of HMF oxidation to FDCA (furandicarboxylic acid) over UT-NiFe and UT-NiMn surface at $U = 1.42$ V versus reversible hydrogen electrode (RHE). M refers to the Ni(Fe) and Ni(Mn) in UT-NiFe and UT-NiMn, respectively, and HMF-OH_2 and FFCA-OH_2 stand for their geminal diol form in pH = 14 alkaline solution.

changes observed. Therefore, as shown in the schematic illustration (Figure S45, Supporting Information), Ni–O and Mn–O sites in UT-NiMn electrocatalyst function as dual active sites during HMFOR for the aldehyde-group-favored HAT mechanism and the alcohol-group-favored EPT mechanism, respectively.[6]

6. Alteration of Deprotonation Capability by Electronic Structure

To understand the enhanced performance and origin of the high deprotonation propensity of UT-LDHs, the electronic structures of LDHs and UT-LDHs were further examined by NEXAFS (**Figure 5**a–d). As NEXAFS is sensitive to the valence state and geometry, the valence states of Ni, Fe, and Mn are determined by comparing the spectral shapes and peak positions of Ni, Fe, and Mn L-edges with octahedral hydrotalcite structures. The Ni and Fe of both UT-NiFe and NiFe LDHs have an oxidation state of 2^+ and 3^+, respectively.[15a] The Ni in UT-NiMn and NiMn LDHs shows the same valence state of 2^+; however, the Mn shows a mixed $2^+/3^+$ valence state, commonly reported in layered Mn oxides.[30b] Due to the double exchange effect, the coexistence of Mn^{2+} and Mn^{3+} endows UT-NiMn with better electron transport properties, where electrons could easily hop and delocalize between $3d^5$ ($t_{2g}{}^3e_g{}^2$) Mn^{3+} and $3d^4$($t_{2g}{}^3e_g{}^3$) Mn^{3+} via bridging O.[37]

XAS measurements of the O K-edge offer a rationale for the relationship between the catalyst performance and transition metal (TM)–O hybridization level. The pre-edge of the O K-edge (Figure 5d, light blue region) is regarded as a key indicator of the hybridization level of TM 3d and O 2p orbitals, and the extent of hybridization is proportional to the intensity of the pre-edge features.[38] As shown in Figure 5a and Figure S46 (Supporting Information), the t_{2g} peaks of Ni^{2+} in the Ni L-edge spectra of UT-LDHs display a sharp drop in peak intensity compared to their bulk counterparts. Correspondingly, increased intensity could be observed at their t_{2g}^* features of Ni^{2+} in the pre-edge region of the O K-edge, indicating electron transfer from the O 2p orbital to the t_{2g} orbital of Ni^{2+} (Figure 5e). Similar trends can be seen in the spectra of Fe L-edge, Mn L-edge, and their corresponding O K-pre-edge, showing decreased peak intensities at both of their t_{2g} and e_g peaks and increased intensities at Fe^{3+} t_{2g}^* and e_g^*, and Mn^{2+}/Mn^{3+} t_{2g}^* and e_g^* peaks (Figure 5b,c,e). The above findings indicate the interfacial electron transfer and formation of low-valence M, or to say, the $M^{(n-\delta)+} - O^{(n+\delta)-}$ ($n = 2$ or 3) couple in UT-LDHs, which further facilitates the formation of oxygen vacancies, as previously observed in hard X-ray XAS.[39] Detailed fitting results are shown in Table S3 (Supporting Information). Further, the analysis of integrated O K-pre-edge areas reflecting the hybridization level of TM–O shows a strong correlation with the overall performance of HMF conversion to FDCA (Figure 5f). With enhanced M 3d-O 2p hybridization, the M–O bond acquires higher electron density/covalency along the more electronegative M site, lowering the covalency of the neighboring O–H through the inductive effect and thus decreasing the energy required for the deprotonation process of UT-LDHs.[40] Consequently, UT-LDHs show a lower onset potential and a larger working potential window for HMF conversion. Moreover, the oxygen holes generated on the O 2p orbitals due to strong hybridization turn the magnetic ground state of UT-LDHs from antiferromagnetic to ferromagnetic. This is especially the case for UT-NiMn with a negative charge transfer energy, endowing UT-LDHs with much higher electrical conductivity and charge transfer ability than non-UT materials.[41]

DFT calculations were conducted on the thermodynamic activity of UT-NiFe and UT-NiMn toward the full reaction pathway of HMF to FDCA conversion. The results confirm that the steps involving electrogeneration of MOOH generally exhibit an energetically uphill process for UT-NiMn and UT-NiFe, while the oxidation of biomass substrates on the electrogenerated catalyst surface are all spontaneous reactions (Figure 5g). During the initial catalyst deprotonation step (Figure S47, Supporting Information), UT-NiFe has a barrier energy of 2.31 eV to overcome deprotonation and transfer into its oxyhydroxide. However, UT-NiMn requires a significantly smaller energy (1.49 eV) to be converted into its oxyhydroxide. Furthermore, UT-NiMn demonstrates 0.82 and 0.81 eV lower barrier energy than UT-NiFe for the conversion reaction of HMFCA to FFCA, and FFCA to FDCA, respectively. The lower barrier energy for the reaction on UT-NiMn is attributed to the stronger M–O bond and weaker O–H bond compared with UT-NiFe, as shown in their isosurfaces of electron density distribution (Figures S48 and S49, Supporting Information), which is consistent with the above XAS O K-edge results (Figure 5d).

7. Conclusion

By combining a suite of in situ X-ray based techniques and potential dependent electrochemical characterizations, the imperative role of enriched deprotonated sites on Ni-based UT-LDHs as electron and proton acceptors in highly selective and fast-kinetics HMFOR is comprehensively revealed. Notably, the deprotonation ability of M–O sites in LDHs can be effectively tuned by introducing defects into the material structure, thereby facilitating an internal electron density redistribution and correspondingly enhancing the covalency along the M–O sites and weakening the O–H bonds. Further, in the UT-NiMn system, the concurrent deprotonation of Ni–OH and Mn–OH active sites and distinct functions of Ni–O and Mn–O sites as dual active sites for respective aldehyde and alcohol groups on HMF are clarified from the viewpoint of their different electronic structure changes during HMFOR, which effectively avoids the competition between active sites. The work establishes a new platform for designing highly efficient next-generation electrocatalysts for HMFOR through rationally engineering the materials' deprotonation ability. It offers a universal guideline to promote other primary alcohol/aldehyde organic oxidation reactions in hybrid water electrolysis systems for renewable-energy generation and mass production of clean fuels and chemicals.

Supporting Information

Supporting Information is available from the Wiley Online Library or from the author.

Acknowledgements

Y.Y. would like to acknowledge scholarship support funded by the Faculty of Engineering at UNSW and the Australian Renewable Energy Agency (ARENA) Hydrogen Program (2018/RND015). XAS and ex situ HE-XRD measurements were performed at the 10-ID-B and 11-ID-B beamlines of the Advanced Photon Source respectively, a U.S. Department of Energy (DOE) Office of Science User Facility, operated for the DOE Office of Science by Argonne National Laboratory under Contract No. DE-AC02-06CH11357. This research used the mail-in program 11-ID-B, while operations at 10-ID-B were further supported by the Materials Research Collaborative Access Team and its member institutions. The authors would like to thank Dr. Joshua Wright for his assistance at 10-ID-B. The soft X-ray spectroscopy experiment was undertaken on the SXR beamline at the Australian Synchrotron, part of ANSTO, and the authors would like to thank Dr. Bruce Cowie, the principal scientist of SXR, for his generous help in the experiments. The authors acknowledge DESY (Hamburg, Germany), a member of the Helmholtz Association (HGF) for the provision of PETRA-III for in situ electrocatalytic PDF measurements performed at the P21 beamline under proposal I-20200433. The authors would like to thank Dr. Soham Banerjee, Dr. Philipp Glaevecke, and Dr. Ann-Christin Dippel for assistance in using beamline P21. The authors acknowledge the European Synchrotron Radiation Facility (ESRF) for provision of synchrotron radiation facilities, and they would like to thank Dr. Blanka Detlefs for assistance and support in using the ID26 beamline for XAS measurements and Mrs. Haira Hackbarth for sample preparation support. The authors acknowledge the use of the facilities and the scientific and technical assistance of the ORNL's Center for Nanophase Materials Sciences (CNMS), Mark Wainwright Analytical Centre (MWAC), and the Electron Microscope Unit (EMU) at UNSW, Sydney. N.M.B would like to acknowledge support from the UNSW Digital Grid Futures Institute. The financial support by the federal ministry for education and research (Bundesministerium für Bildung

und Forschung, BMBF) under Grant Numbers 03SF0613D "AEMready", 03HY108D "HyThroughGen" and 03HY3002Q "H2Mare" are gratefully acknowledged. The research was undertaken with the assistance of computational resources provided by National Computational Infrastructure (NCI) Australia.

Open access publishing facilitated by University of New South Wales, as part of the Wiley - University of New South Wales agreement via the Council of Australian University Librarians.

Conflict of Interest

The authors declare no conflict of interest.

Data Availability Statement

The data that support the findings of this study are available from the corresponding author upon reasonable request.

Keywords

biomass electrooxidation, defective engineering, electron transfer processes, metal-oxygen covalency, Ni-based layered double hydroxide, structural evolution, proton transfer processes

Received: June 10, 2023
Revised: September 15, 2023
Published online:

[1] a) Y. Yang, Y. Yang, Z. Pei, K.-H. Wu, C. Tan, H. Wang, L. Wei, A. Mahmood, C. Yan, J. Dong, S. Zhao, Y. Chen, *Matter* **2020**, *3*, 1442; b) K. R. Vuyyuru, P. Strasser, *Catal. Today* **2012**, *195*, 144.

[2] a) B. You, Y. Sun, *Acc. Chem. Res.* **2018**, *51*, 1571; b) P. Gu, S. Zhang, X. Li, X. Wang, T. Wen, R. Jehan, A. Alsaedi, T. Hayat, X. Wang, *Environ. Pollut.* **2018**, *240*, 493; c) Y. Yang, Y. Yang, Y. Liu, S. Zhao, Z. Tang, *Small Sci.* **2021**, *1*, 2100015; d) P. Hauke, M. Klingenhof, X. Wang, J. F. De Araújo, P. Strasser, *Cell Rep. Phys. Sci.* **2021**, *2*, 100650.

[3] a) M. E. Zakrzewska, E. Bogel-Lukasik, R. Bogel-Lukasik, *Chem. Rev.* **2011**, *111*, 397; b) W. H. Lie, Y. Yang, J. A. Yuwono, C. Tsounis, M. Zubair, J. Wright, L. Thomsen, P. Kumar, N. Bedford, *J. Mater. Chem. A* **2023**, *11*, 5527.

[4] a) S. Barwe, J. Weidner, S. Cychy, D. M. Morales, S. Dieckhöfer, D. Hiltrop, J. Masa, M. Muhler, W. Schuhmann, *Angew. Chem., Int. Ed.* **2018**, *57*, 11460; b) W.-J. Liu, L. Dang, Z. Xu, H.-Q. Yu, S. Jin, G. W. Huber, *ACS Catal.* **2018**, *8*, 5533; c) L. Gao, Z. Liu, J. Ma, L. Zhong, Z. Song, J. Xu, S. Gan, D. Han, L. Niu, *Appl. Catal., B* **2020**, *261*, 118235.

[5] a) M. Fleischmann, K. Korinek, D. Pletcher, *J. Electroanal. Chem. Interfacial Electrochem.* **1971**, *31*, 39; b) M. Fleischmann, K. Korinek, D. Pletcher, *J. Chem. Soc., Perkin Trans. 2* **1972**, 1396; c) B. Mondal, N. Karjule, C. Singh, R. Shimoni, M. Volokh, I. Hod, M. Shalom, *Adv. Energy Mater.* **2021**, *11*, 2101858; d) Y. Yang, T. Mu, *Green Chem.* **2021**, *23*, 4228; e) W. Chen, C. Xie, Y. Wang, Y. Zou, C.-L. Dong, Y.-C. Huang, Z. Xiao, Z. Wei, S. Du, C. Chen, B. Zhou, J. Ma, S. Wang, *Chem* **2020**, *6*, 2974; f) M. T. Bender, Y. C. Lam, S. Hammes-Schiffer, K.-S. Choi, *J. Am. Chem. Soc.* **2020**, *142*, 21538.

[6] M. T. Bender, R. E. Warburton, S. Hammes-Schiffer, K.-S. Choi, *ACS Catal.* **2021**, *11*, 15110.

[7] B. J. Taitt, D.-H. Nam, K.-S. Choi, *ACS Catal.* **2018**, *9*, 660.

[8] Y. Yang, S. Zhao, *Chem Catal.* **2023**, *3*, 100529.

[9] a) M. Zhang, Y. Liu, B. Liu, Z. Chen, H. Xu, K. Yan, *ACS Catal.* **2020**, *10*, 5179; b) W. Chen, B. Wu, Y. Wang, W. Zhou, Y. Li, T. Liu, C. Xie, L. Xu, S. Du, M. Song, D. Wang, Y. Liu, Y. Li, J. Liu, Y. Zou, R. Chen, C. Chen, J. Zheng, Y. Li, J. Chen, S. Wang, *Energy Environ. Sci.* **2021**, *14*, 6428; c) M. Klingenhof, P. Hauke, M. Kroschel, X. Wang, T. Merzdorf, C. Binninger, T. Ngo Thanh, B. Paul, D. Teschner, R. Schlögl, P. Strasser, *ACS Energy Lett.* **2022**, *7*, 3415.

[10] a) P. M. Bodhankar, P. B. Sarawade, G. Singh, A. Vinu, D. S. Dhawale, *J. Mater. Chem. A* **2021**, *9*, 3180; b) S. Dresp, T. Ngo Thanh, M. Klingenhof, S. Brückner, P. Hauke, P. Strasser, *Energy Environ. Sci.* **2020**, *13*, 1725; c) Z. Qiu, C.-W. Tai, G. A. Niklasson, T. Edvinsson, *Energy Environ. Mater.* **2019**, *12*, 572; d) F. Dionigi, J. Zhu, Z. Zeng, T. Merzdorf, H. Sarodnik, M. Gliech, L. Pan, W.-X. Li, J. Greeley, P. Strasser, *Angew. Chem., Int. Ed.* **2021**, *133*, 14567; e) F. Dionigi, Z. Zeng, I. Sinev, T. Merzdorf, S. Deshpande, M. B. Lopez, S. Kunze, I. Zegkinoglou, H. Sarodnik, D. Fan, A. Bergmann, J. Drnec, J. F. De Araujo, M. Gliech, D. Teschner, J. Zhu, W.-X. Li, J. Greeley, B. R. Cuenya, P. Strasser, *Nat. Commun.* **2020**, *11*, 2522.

[11] a) Y. Tang, H. Shen, J. Cheng, Z. Liang, C. Qu, H. Tabassum, R. Zou, *Adv. Funct. Mater.* **2020**, *30*, 1908223; b) X. Guo, T. Zheng, G. Ji, N. Hu, C. Xu, Y. Zhang, *J. Mater. Chem. A* **2018**, *6*, 10243.

[12] S. Zhao, Y. Yang, Z. Tang, *Angew. Chem., Int. Ed.* **2022**, *134*, e202110186.

[13] a) Y. Zhao, X. Zhang, X. Jia, G. I. N. Waterhouse, R. Shi, X. Zhang, F. Zhan, Y. Tao, L.-Z. Wu, C.-H. Tung, D. O'hare, T. Zhang, *Adv. Energy Mater.* **2018**, *8*, 1703585; b) J. Yu, B. R. Martin, A. Clearfield, Z. Luo, L. Sun, *Nanoscale* **2015**, *7*, 9448.

[14] a) F. L. Theiss, G. A. Ayoko, R. L. Frost, *Appl. Surf. Sci.* **2016**, *383*, 200; b) Q. Wang, D. O'hare, *Chem. Rev.* **2012**, *112*, 4124.

[15] a) J. Jiang, F. Sun, S. Zhou, W. Hu, H. Zhang, J. Dong, Z. Jiang, J. Zhao, J. Li, W. Yan, *Nat. Commun.* **2018**, *9*, 2885; b) M. Gong, Y. Li, H. Wang, Y. Liang, J. Z. Wu, J. Zhou, J. Wang, T. Regier, F. Wei, H. Dai, *J. Am. Chem. Soc.* **2013**, *135*, 8452.

[16] G. Manohara, *RSC Adv.* **2014**, *4*, 46126.

[17] J. Shin, C.-J. Choi, T.-H. Kim, J.-M. Oh, Design, *J. Cryst. Growth* **2018**, *18*, 5398.

[18] V. Petkov, *Mater. Today* **2008**, *11*, 28.

[19] S. Zhao, C. Tan, C.-T. He, P. An, F. Xie, S. Jiang, Y. Zhu, K.-H. Wu, B. Zhang, H. Li, J. Zhang, Y. Chen, S. Liu, J. Dong, Z. Tang, *Nat. Energy* **2020**, *5*, 881.

[20] A. S. Batchellor, G. Kwon, F. A. L. Laskowski, D. M. Tiede, S. W. Boettcher, *J. Phys. Chem. C* **2017**, *121*, 25421.

[21] Q. Zhang, X. He, J. Shi, N. Lu, H. Li, Q. Yu, Z. Zhang, L.-Q. Chen, B. Morris, Q. Xu, *Nat. Commun.* **2017**, *8*, 1.

[22] M. Kotiuga, Z. Zhang, J. Li, F. Rodolakis, H. Zhou, R. Sutarto, F. He, Q. Wang, Y. Sun, Y. Wang, N. A. Aghamiri, S. B. Hancock, L. P. Rokhinson, D. P. Landau, Y. Abate, J. W. Freeland, R. Comin, S. Ramanathan, K. M. Rabe, *Proc. Natl. Acad. Sci. U. S. A.* **2019**, *116*, 21992.

[23] a) Z. Zhang, H. Huo, L. Wang, S. Lou, L. Xiang, B. Xie, Q. Wang, C. Du, J. Wang, G. Yin, *Chem. Eng. J.* **2021**, *412*, 128617; b) Y. Tong, J. Wu, P. Chen, H. Liu, W. Chu, C. Wu, Y. Xie, *J. Am. Chem. Soc.* **2018**, *140*, 11165.

[24] a) R. Lin, L. Kang, T. Zhao, J. Feng, V. Celorrio, G. Zhang, G. Cibin, A. Kucernak, D. J. L. Brett, F. Corà, I. P. Parkin, G. He, *Energy Environ. Sci.* **2022**, *15*, 2386. b) N. K. Shrestha, S. A. Patil, A. S. Salunke, A. I. Inamdar, H. Im, *J. Mater. Chem. A* **2023**, *11*, 14870.

[25] T. Hayashi, N. Bonnet-Mercier, A. Yamaguchi, K. Suetsugu, R. Nakamura, *R. Soc. Open Sci.* **2019**, *6*, 190122.

[26] Y. Sun, J. Wang, Y. Qi, W. Li, C. Wang, *Adv. Sci.* **2022**, *9*, 2200957.

[27] W. Cheng, S. Xi, Z.-P. Wu, D. Luan, X. W. Lou, *Sci. Adv.* **2021**, *7*, eabk0919.

[28] a) T. Kohler, T. Armbruster, E. Libowitzky, *J. Solid State Chem.* **1997**, *133*, 486; b) A. Jain, S. P. Ong, G. Hautier, W. Chen, W. D. Richards, S. Dacek, S. Cholia, D. Gunter, D. Skinner, G. Ceder, *APL Mater.* **2013**, *1*, 011002.

[29] A. M. Bystrom, *Acta Chim. Sin.* **1949**, *3*, 163.
[30] a) Y. Meng, W. Song, H. Huang, Z. Ren, S.-Y. Chen, S. L. Suib, *J. Am. Chem. Soc.* **2014**, *136*, 11452; b) M. Risch, K. A. Stoerzinger, B. Han, T. Z. Regier, D. Peak, S. Y. Sayed, C. Wei, Z. Xu, Y. Shao-Horn, *J. Phys. Chem. C* **2017**, *121*, 17682.
[31] M. Görlin, P. Chernev, J. Ferreira De Araújo, T. Reier, S. Dresp, B. Paul, R. Krähnert, H. Dau, P. Strasser, *J. Am. Chem. Soc.* **2016**, *138*, 5603.
[32] F. Frati, M. O. J. Y. Hunault, F. M. F. De Groot, *Chem. Rev.* **2020**, *120*, 4056.
[33] C. Kuai, Z. Xu, C. Xi, A. Hu, Z. Yang, Y. Zhang, C.-J. Sun, L. Li, D. Sokaras, C. Dong, S.-Z. Qiao, X.-W. Du, F. Lin, *Nat. Catal.* **2020**, *3*, 743.
[34] a) Y. Lu, T. Liu, Y.-C. Huang, L. Zhou, Y. Li, W. Chen, L. Yang, B. Zhou, Y. Wu, Z. Kong, Z. Huang, Y. Li, C.-L. Dong, S. Wang, Y. Zou, *ACS Catal.* **2021**, *12*, 4242; b) G. Li, Q. Yang, J. Rao, C. Fu, S. C. Liou, G. Auffermann, Y. Sun, C. Felser, *Adv. Funct. Mater.* **2020**, *30*, 1907791; c) B.-A. Mei, J. Lau, T. Lin, S. H. Tolbert, B. S. Dunn, L. Pilon, *J. Phys. Chem. C* **2018**, *122*, 24499; d) Y. Lu, T. Liu, C.-L. Dong, C. Yang, L. Zhou, Y.-C. Huang, Y. Li, B. Zhou, Y. Zou, S. Wang, *Adv. Mater.* **2022**, *34*, 2107185.
[35] Z. Xiao, Y.-C. Huang, C.-L. Dong, C. Xie, Z. Liu, S. Du, W. Chen, D. Yan, L. Tao, Z. Shu, G. Zhang, H. Duan, Y. Wang, Y. Zou, R. Chen, S. Wang, *J. Am. Chem. Soc.* **2020**, *142*, 12087.
[36] W. Chen, Y. Wang, B. Wu, J. Shi, Y. Li, L. Xu, C. Xie, W. Zhou, Y.-C. Huang, T. Wang, S. Du, M. Song, D. Wang, C. Chen, J. Zheng, J. Liu, C.-L. Dong, Y. Zou, J. Chen, S. Wang, *Adv. Mater.* **2022**, *34*, 2105320.
[37] X. Zhong, M. h. Oubla, X. Wang, Y. Huang, H. Zeng, S. Wang, K. Liu, J. Zhou, L. He, H. Zhong, *Nat. Commun.* **2021**, *12*, 3136.
[38] a) F. Frati, M. O. J. Y. Hunault, F. M. F. De Groot, *Chem. Rev.* **2020**, *120*, 4056; b) S. Roychoudhury, R. Qiao, Z. Zhuo, Q. Li, Y. Lyu, J. H. Kim, J. Liu, E. Lee, B. J. Polzin, J. Guo, *Energy Environ. Mater.* **2021**, *4*, 246; c) J. Suntivich, W. T. Hong, Y.-L. Lee, J. M. Rondinelli, W. Yang, J. B. Goodenough, B. Dabrowski, J. W. Freeland, Y. Shao-Horn, *J. Phys. Chem. C* **2014**, *118*, 1856.
[39] a) Y. Yao, Y. Zhu, C. Pan, C. Wang, S. Hu, W. Xiao, X. Chi, Y. Fang, J. Yang, H. Deng, S. Xiao, J. Li, Z. Luo, Y. Guo, *J. Am. Chem. Soc.* **2021**, *143*, 8720; b) G. Liang, E. Olsson, J. Zou, Z. Wu, J. Li, C.-Z. Lu, A. M. D'angelo, B. Johannessen, L. Thomsen, B. Cowie, V. K. Peterson, Q. Cai, W. K. Pang, Z. Guo, *Angew. Chem., Int. Ed.* **2022**, *61*, e202201969.
[40] H. Liu, J. Zhou, L. Zhang, Z. Hu, C. Kuo, J. Li, Y. Wang, L. H. Tjeng, T.-W. Pi, A. Tanaka, L. Song, J.-Q. Wang, S. Zhang, *J. Phys. Chem. C* **2017**, *121*, 16079.
[41] S. Chowdhury, A. Jana, M. Kuila, V. R. Reddy, R. J. Choudhary, D. Phase, *ACS Appl. Electron. Mater.* **2020**, *2*, 3859.